

THE OFFICIAL MAGAZINE OF THE OCEANOGRAPHY SOCIETY

Oceanography

CITATION

Lowell, R.P., A. Farough, L.N. Germanovich, L.B. Hebert, and R. Horne. 2012.
A vent-field-scale model of the East Pacific Rise 9°50'N magma-hydrothermal system.
Oceanography 25(1):158–167, <http://dx.doi.org/10.5670/oceanog.2012.13>.

DOI

<http://dx.doi.org/10.5670/oceanog.2012.13>

COPYRIGHT

This article has been published in *Oceanography*, Volume 25, Number 1, a quarterly journal of The Oceanography Society. Copyright 2012 by The Oceanography Society. All rights reserved.

USAGE

Permission is granted to copy this article for use in teaching and research. Republication, systematic reproduction, or collective redistribution of any portion of this article by photocopy machine, reposting, or other means is permitted only with the approval of The Oceanography Society. Send all correspondence to: info@tos.org or The Oceanography Society, PO Box 1931, Rockville, MD 20849-1931, USA.



A Vent-Field-Scale Model of the East Pacific Rise 9°50'N Magma-Hydrothermal System

BY ROBERT P. LOWELL, AIDA FAROUGH, LEONID N. GERMANOVICH,
LAURA B. HEBERT, AND REBECCA HORNE

ABSTRACT. This paper describes a two-limb single-pass modeling approach constrained by vent temperature, heat flow, vent geochemistry, active-source seismology, and seismically inferred circulation geometry to provide first-order constraints on crustal permeability, conductive boundary layer thickness, fluid residence times, and magma replenishment rates for the magma-hydrothermal system at the East Pacific Rise (EPR) near 9°50'N. Geochemical data from black smokers and nearby diffuse-flow patches, as well as an estimate of heat flow partitioning, suggest that nearly 90% of the heat output stems from heat supplied by the subaxial magma chamber, even though almost 90% of that output appears as diffuse flow at the seafloor. Estimates of magma replenishment rates are consistent with the evolution of lava chemistry over the eruption cycle between 1991–1992 and 2005–2006. If the recharge surface area is 10^5 m², a one-dimensional model of hydrothermal recharge using EPR 9°50'N parameters gives rise to rapid sealing as a result of anhydrite precipitation; however, if the area of recharge widens at depth to $\sim 10^6$ m², sealing by anhydrite precipitation may not significantly affect hydrothermal circulation.

INTRODUCTION

The East Pacific Rise (EPR) between 8° and 11°N, with particular emphasis on a “bull’s-eye” region near 9°50'N, has been the subject of extensive research for more than two decades (Fornari et al., 2012, in this issue). As a designated Ridge 2000 Integrated Study Site, a particular goal has been to use the available multidisciplinary data sets to construct an integrated, quantitative

model of magma-hydrothermal processes at EPR 9°50'N. However, this overarching goal is beyond present-day scientific capabilities. We have a limited amount of heat output data; we lack a sound understanding of the mechanics of magma transport within the crust and upper mantle, crustal assimilation, and mixing within the axial magma chamber (AMC); and we have insufficient knowledge of detailed subsurface

hydrology and biogeochemical processes to develop fully integrated models. By using a vent-field-scale analysis approach, however, we employ a number of data sets to constrain a simple, yet robust, parametric mathematical model. This modeling approach is designed to provide a basic framework for the next generation of numerical models and to guide future research at this important natural laboratory.

In this article, we summarize the multiple data sets that are available to constrain mathematical and numerical models. These data include observations of temperature and hydrothermal heat output from both black smoker and diffuse-flow sites, vent fluid geochemistry, geophysics, detailed seafloor mapping, and analyses of erupted lavas from the 1991–1992 and the 2005–2006 eruptions. Then, we develop the hydrothermal circulation model in terms of three main elements: (1) a discharge zone, where heated fluids ascend from near the top of a subsurface AMC and vent at the seafloor with temperatures

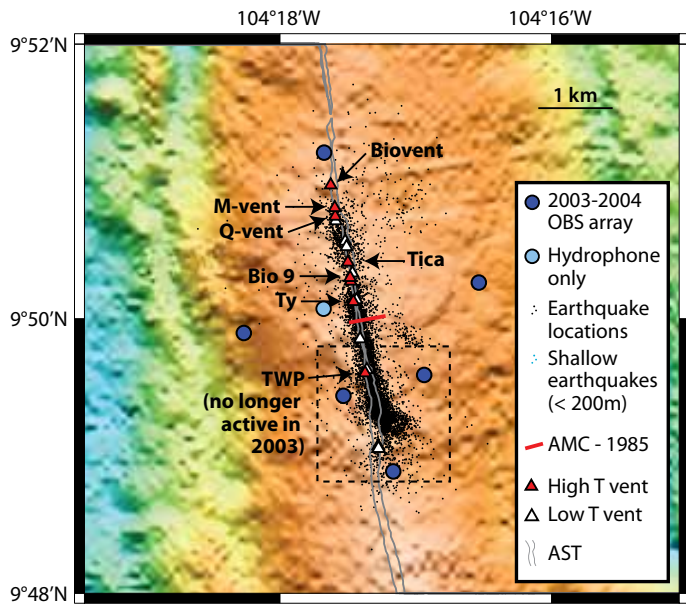


Figure 1. Map view of the EPR 9°50'N hydrothermal field showing high- and low-temperature vents. This region is referred to as the “bull’s-eye” of the EPR Integrated Study Site. The black dots are the epicenters of 7,000 microearthquakes recorded in a seven-month study; the dashed box is the postulated recharge zone. From Tolstoy et al. (2008), reprinted by permission from Macmillan Publishers Ltd.

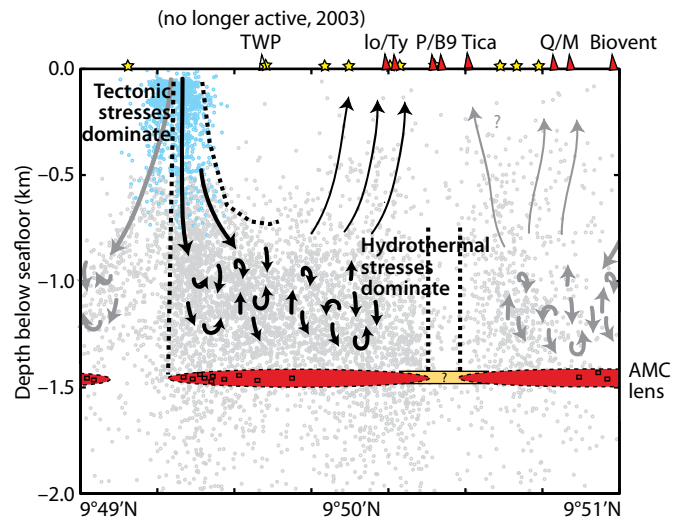


Figure 2. Schematic of inferred hydrothermal convection cells at EPR 9°50'N. The red ellipses denote the axial magma chamber (AMC), and the gray and blue dots denote earthquake locations. The blue dots are inferred to be shallow tectonic events that delineate the recharge zone. From Tolstoy et al. (2008), reprinted by permission from Macmillan Publishers Ltd.

of ~ 350°–400°C; (2) a heat transfer region near the top of the AMC where heat is transferred from an actively replenished convecting, crystallizing AMC across a thermal conduction boundary layer to the circulating fluid; and (3) a recharge zone, where seawater enters the crust and percolates to near the top of the magma chamber. In addition to these three main hydrothermal flow elements, we consider thermally induced circulation within seismic Layer 2A (uppermost part of the oceanic crust consisting of extrusive lavas). This circulation results in the discharge of low-temperature fluids, generally termed “diffuse flow,” that represents a mixture of seawater and high-temperature hydrothermal fluid (see Bemis et al., 2012, in this issue). We use the term “single-pass” model to describe the circulation system because the fluid passes through it only once.

EPR 9°50'N: CRITICAL OBSERVATIONS AND CONSTRAINING DATA

At the EPR bull’s-eye centered at 9°50'N, a number of vents, from Biovent in the north to Tube Worm Pillar (TWP) in the south (Figure 1), delineate a ~ 2 km long hydrothermal discharge zone that, based on seismicity and seismic reflection data, can be represented with two along-axis convection cells (e.g., Tolstoy et al., 2008). One cell extends from the Bio 9–P vent area to TWP in the south; the other extends to Biovent in the

north (Figure 2). The vents are generally located along the axial summit trough (AST), which varies in width from 40 to 100 m (Ferrini et al., 2007). Figures 1 and 2 show a seismically inferred recharge zone that feeds the circulation cell between TWP and the Bio 9 vent area and occupies a seafloor area of ~ 10⁵ m².

Ramondenc et al. (2006) indicate that heat output from the region between TWP and Bio 9 (Figures 1 and 2) is ~ 160 MW, with ~ 20 MW from black smoker vents and ~ 140 MW from

Robert P. Lowell (rlowell@vt.edu) is Research Professor, Department of Geosciences, Virginia Tech, Blacksburg, VA, USA. **Aida Farough** is a PhD candidate in the Department of Geosciences, Virginia Tech, Blacksburg, VA, USA. **Leonid N. Germanovich** is Professor, School of Civil and Environmental Engineering, Georgia Institute of Technology, Atlanta, GA, USA. **Laura B. Hebert** is Assistant Research Scientist, Department of Geology, University of Maryland, College Park, MD, USA. **Rebecca Horne** was an undergraduate in the Department of Geosciences, Virginia Tech, Blacksburg, VA, and is currently an MS candidate in the School of Geology and Geophysics, University of Oklahoma, Norman, OK, USA.

Table 1. List of observables and parameter values used

	Symbol	Definition	Value	Units
OBSERVABLES	A_d	Area of discharge zone	10^3 – 10^4	m ²
	A_m	Cross-sectional surface area of axial magma chamber	10^6	m ²
	A_r	Area of recharge zone	10^5 – 10^6	m ²
	h	Depth of axial magma chamber	1.5×10^3	m
	H	Total heat output	$160 \pm 50\%$	MW
	H_3	High-temperature heat output at seafloor	20	MW
	H_4	Diffuse heat output at seafloor	$140 \pm 50\%$	MW
	Mg_{sw}	Magnesium concentration in sw	52.2	mmol kg ⁻¹
	Mg_{ht}	Magnesium concentration in black smoker fluid	0	mmol kg ⁻¹
	Mg_{diff}	Average magnesium concentration in diffuse flow	49.2	mmol kg ⁻¹
	T_3	Average black smoker temperature	370	°C
	T_4	Average diffuse flow temperature	30	°C
PARAMETERS	a^*	Effective thermal diffusivity	10^{-6}	m ² s ⁻¹
	c_{ht}	Specific heat of fluid at high temperature	5×10^3	J kg ⁻¹
	c_{lt}	Specific heat of fluid at low temperature	4×10^3	J kg ⁻¹
	dC_{eq}/dT	Derivative of equilibrium concentration of anhydrite with temperature	1.8×10^{-4}	°C ⁻¹
	g	Acceleration due to gravity	9.8	m s ⁻²
	k_d	Permeability of discharge zone		m ²
	Q	Mass flow rate		kg s ⁻¹
	t_s	Sealing time resulting from anhydrite precipitation		s
	$T_1(z)$	Temperature distribution in recharge zone		°C
	T_b	Temperature at base of recharge zone	300	°C
	T_1	Temperature in recharge zone	0	°C
	u	Vertical Darcian velocity		m s ⁻¹
	\dot{V}_m	Magma replenishment rate		m ³ yr ⁻¹
	α_d	Thermal expansion coefficient of fluid	10^{-3}	1/°C
	δ	Thickness of conductive boundary layer		m
	ϕ	Porosity	0.01–0.1	
	λ	Thermal conductivity of boundary layer	2.0	W m ⁻¹ °C
	ν_d	Kinematic viscosity of fluid	10^{-7}	m ² s ⁻¹
	ρ_s	Anhydrite mineral density	2,500	kg m ⁻³
	ρ_f	Fluid density	700–1,000	kg m ⁻³
τ	Fluid residence time		s	
ξ	Mixing fraction of high-temperature fluid in diffuse flow			
χ	Concentration of conservative tracer			

diffuse flow. These heat output data are uncertain by about a factor two, (Ramondenc et al., 2006), most of which is associated with uncertainty in the diffuse-flow component. The magnitude of uncertainty in hydrothermal heat output is similar to that at other sites regardless of measurement technique (Baker, 2007). Despite the large uncertainty in the data, the measured heat output is typical of many mid-ocean ridge hydrothermal systems (e.g., Ramondenc et al., 2006; Baker, 2007). Table 1 lists the key observational data used to constrain the model and other parameters.

Lengthy time series of temperature measurements are available for many of the vents and diffuse-flow areas near EPR 9°50'N (e.g., Von Damm and Lilley, 2004). Between 1991 and 2000, the average temperature of the Bio 9 complex, which includes Bio 9, Bio 9', and P vents, is approximately 370°C, whereas the average temperature of diffuse flow near these vents (Figure 1) is approximately 30°C (Von Damm and Lilley, 2004).

Many of the vents near EPR 9°50'N have been sampled repeatedly for water chemistry. Although these data have not been incorporated into reactive transport models of hydrothermal circulation at this site, the data have been used to elucidate various subseafloor processes. The Cl data provide evidence of phase separation in the hydrothermal system. Repeat measurements at closely spaced vents such as Bio 9, Bio 9', and P show that they exhibit remarkable differences in Cl and simultaneous venting of vapor- and brine-derived fluids as a function of time (Von Damm, 2004; Figure 3). In addition, geochemical data from high-temperature

vents and nearby diffuse-flow sites have been used to estimate rates of subsurface biological activity (Crowell et al., 2008) and to determine the partitioning of heat flow between high-temperature vents and diffuse flow (Craft and Lowell, 2009; Germanovich et al., 2011; see The Discharge Zone section below).

Seismic reflection data (Detrick et al., 1987) place the AMC at a depth of ~ 1.5 km below the seafloor with a variable across-axis extent of ~ 1 km. Results from a recent three-dimensional multichannel seismic survey (Carbotte et al., 2011) suggest that there are strong correlations among AMC depth, ridge segmentation, and volume of the axial high, and that undulation of ~ 100 m in AMC depth may occur on scales of a few kilometers along the axis. These features are consistent with multiple episodes of focused magma replenishment. The AMC is estimated to be several tens of meters thick (Kent et al., 1990).

Magmatic activity and seismicity, and their links to vent temperatures, provide key insights into magma-hydrothermal coupling at EPR 9°50'N. Eruptions in

1991–1992 and again in 2005–2006 have provided a suite of lavas whose chemistry can be used to investigate AMC cooling, fractionation, and replenishment over an eruption cycle (Goss et al., 2010, and see the Magmatic Heat Transfer and Magma Replenishment section below). Seismic swarms followed by rapid changes in vent temperature (e.g., Sohn et al., 1998) may provide constraints on hydrothermal plumbing and may be related to non-eruptive diking events (e.g., Germanovich et al., 2011).

MODEL DEVELOPMENT AND RESULTS

Figure 4 depicts the main elements of a single-pass circulation model above a convecting AMC. The deep recharge zone on the left is a one-dimensional representation of the along-axis recharge zone postulated by Tolstoy et al. (2008). The area on the right depicts two regimes: (1) a deep discharge zone connected to a deep recharge zone by a cross-flow zone, and (2) a shallow circulation cell within which seawater and high-temperature fluid mix, resulting in low-temperature

diffuse flow. The depth of this mixing zone is not well defined, but is likely to be confined mainly to seismic Layer 2A (e.g., Germanovich et al., 2011).

The Discharge Zone

We begin by using the heat flow, temperature, and geochemical data from the vent area near Bio 9, Bio 9', and P vents to estimate the mass flow rate, bulk permeability, and thermal boundary layer thickness. Conservation of fluid mass requires that the mass flux Q_1 in the deep recharge zone enters the deep discharge zone. Heat transfer from the AMC raises the temperature from T_1 in the recharge zone to T_3 in the discharge zone (Figure 4). The high-temperature mass flux Q_1 is then divided into two parts. One part, corresponding to Q_3 , vents at the surface at temperature T_3 , giving rise to the black smoker heat flux H_3 . The remainder, $Q_1 - Q_3$, mixes with cold seawater in the shallow limb that has mass flux Q_2 and arrives at the seafloor as diffuse flow Q_4 with a diffuse-flow temperature T_4 and a resultant diffuse-flow heat flux H_4 . The mass fluxes Q_3 and Q_4 can be determined directly from the heat flux and temperature data and specific heat using the formulas

$$Q_3 = \frac{H_3}{c_{ht}T_3}, \quad Q_4 = \frac{H_4}{c_{lt}T_4}, \quad (1)$$

where c_{ht} and c_{lt} are the specific heat of the fluid at high and low temperatures, respectively. Using the values in Table 1, we obtain $Q_3 = 11 \text{ kg s}^{-1}$ and $Q_4 = 1,170 \text{ kg s}^{-1}$, with an uncertainty of a factor of two. Table 2 lists all of the results derived from the model.

We then use Mg concentration as a conservative tracer to obtain the fraction ξ of black smoker fluid entrained in the diffuse flow. We assume that the

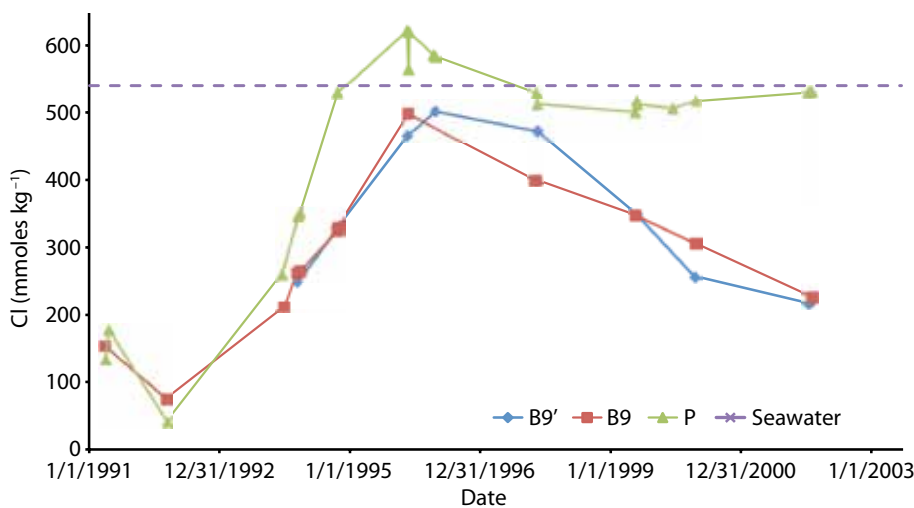


Figure 3. Plot of salinity of Bio 9, Bio 9', and P vents from the EPR 9°50'N between 1991 and 2002. Adapted from Von Damm (2004)

black smoker fluid is an end-member hydrothermal fluid with $Mg = 0$. From Von Damm and Lilley (2004), averages of Mg concentration in diffuse-flow fluid and of seawater near the Bio 9, Bio 9', and P vents are $49.2 \text{ mmol kg}^{-1}$ and $52.2 \text{ mmol kg}^{-1}$, respectively (Craft and Lowell, 2009). Writing the Mg concentration χ , we have

$$\xi = \frac{\chi_{diff} - \chi_{sw}}{\chi_{ht} - \chi_{sw}}, \quad (2)$$

where the subscripts *diff*, *ht*, and *sw* refer to diffuse, high-temperature, and seawater concentrations, respectively. In terms of mass flux, $\xi = (Q_1 - Q_3)/Q_4$, so from

Equations 1 and 2 we can determine the value of Q_1 . We find $\xi = 0.057$ and $Q_1 = 78 \text{ kg s}^{-1}$. Similar results are obtained if we use quartz as the conservative tracer (Craft and Lowell, 2009).

Note that if we had simply assumed that the total heat output $H = 160 \text{ MW}$ resulted from high-temperature heat flux, the value of Q_1 could have been calculated directly using $Q_1 = H/c_{ht}T_3$. In this case, the result is $Q_1 = 86 \text{ kg s}^{-1}$. This value, which we will now call Q_1^* , is only 11% greater than the value of Q_1 determined from heat-flow partitioning. Using the value of $Q_1 = 78 \text{ kg s}^{-1}$ determined from heat-flow partitioning

yields a high-temperature heat output $H_1 = c_{ht}Q_1T_3 = 144 \text{ MW}$. This figure is 90% of the total heat output of 160 MW, and means that even though approximately 88% of the surface heat output appears as diffuse flow, 90% of the total heat output ultimately results from high-temperature fluid rising from near the top of the AMC.

The observed black smoker vent temperature and hydrothermal heat output, together with the calculated value of the mass flux Q_1 and estimates of the planform area of the AMC A_m and hydrothermal vent field A_d , allow estimation of the bulk permeability within the discharge zone, the thickness of the conductive boundary layer at the top of the AMC, and fluid residence time. Table 2 provides these results.

To estimate the bulk permeability k_d of the discharge zone, we assume that the mass flux Q_1 is driven by its thermal buoyancy. Then, using an integrated form of Darcy's Law and assuming the main flow resistance is associated with the discharge limb of the deep convection cell (Lowell and Germanovich, 2004; Germanovich et al., 2011), we obtain that Q_1 scales as

$$Q_1 \approx \frac{\rho_f \alpha_d g (T_3 - T_1) k_d A_d}{\nu_d}, \quad (3)$$

where ρ_f is the fluid density, α_d is the thermal expansion coefficient, g is the acceleration due to gravity, and ν_d is the kinematic viscosity. The area of the discharge zone is between 10^3 and 10^4 m^2 (Germanovich et al., 2011).

Assuming $A_d = 5 \times 10^3 \text{ m}^2$, $T_1 = 0$, and the parameter values in Table 1, we find $k_d = 6 \times 10^{-13} \text{ m}^2$. This result is similar to that estimated from studies on the tidal triggering of earthquakes at EPR 9°50'N (Crone et al., 2011).

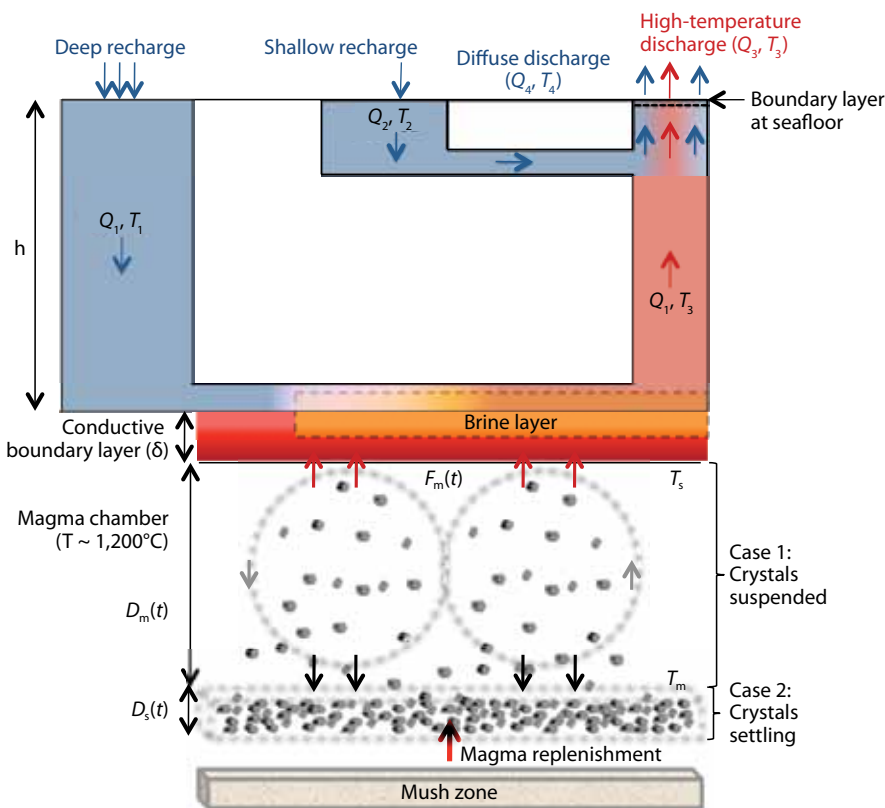


Figure 4. Schematic of a “double-loop” single-pass model above a convecting, crystallizing, replenished axial magma chamber (AMC). Heat transfer $F_m(t)$ from the vigorously convecting, cooling, and replenished AMC across the conductive boundary layer δ drives the overlying hydrothermal system. The deep circulation represented by mass flux Q_1 and black smoker temperature T_3 induces shallow circulation noted by Q_2 . Some black smoker fluid mixes with seawater, resulting in diffuse discharge Q_4, T_4 , while the direct black smoker mass flux with temperature T_3 is reduced from Q_1 to Q_3 . Heat flux, vent temperature, and geochemical data allow estimates of the various mass fluxes.

The value of k_d estimated in the previous paragraph does not take into account the uncertainties in heat output and in the area of the vent field, both of which are significant. Figure 5 plots k_d versus A_d for values of H from 80 to 320 MW, which corresponds to the uncertainty in the total heat output (Ramondenc et al., 2006). The uncertainty in the estimate of k_d highlights the need to obtain better estimates of heat output and area of diffuse flow.

We calculate the average thickness δ of the conductive boundary (Figure 4) by balancing the heat output H_1 from the underlying AMC with the hydrothermal heat output:

$$\frac{\lambda[T_m - (T_3 - T_1)/2]A_m}{\delta} = H_1 = c_{ht}Q_1T_3, \quad (4)$$

where λ is the thermal conductivity of the boundary layer and T_m is the magma temperature. Assuming $T_m = 1,200^\circ\text{C}$, $T_1 = 0$, and $A_m \approx 10^6 \text{ m}^2$, we obtain $\delta = 14 \text{ m}$, with a factor of two uncertainty stemming from the uncertainty in heat output.

The fluid residence time τ in the

discharge zone, which characterizes the rate at which a thermal disturbance is propagated from the AMC to the seafloor, is found simply from the expression

$$\tau = \frac{h}{u}, \quad (5)$$

where h is the length of the travel path and $u = Q_1/\rho_f A_d$ is the vertical Darcian velocity. With $h = 1.5 \text{ km}$, we obtain $7 \times 10^6 \text{ s} \leq \tau \leq 3 \times 10^8 \text{ s}$. The range in residence time reflects the uncertainty in Darcian velocity that stems from the uncertainties in A_d and Q_1 (which is directly proportional to the heat output).

Magmatic Heat Transfer and Magma Replenishment

In the previous section, we equated the observed hydrothermal heat output with the heat transferred across a conductive boundary layer δ between the AMC and the base of the hydrothermal system. Liu and Lowell (2009), however, directly estimate the time-dependent heat flux $F_m(t)$ (Figure 4) from a vigorously convecting, crystallizing AMC and show

that magma replenishment at a rate $\dot{V}_m \sim 2 \times 10^6 \pm 50\% \text{ m}^3 \text{ yr}^{-1}$ is required to maintain stable hydrothermal temperatures and heat outputs on decadal time scales. This replenishment rate is about three times faster than the mean rate of crustal production ($\sim 6 \times 10^5 \text{ m}^3 \text{ yr}^{-1}$ per kilometer of ridge axis for 6 km thick crust at the EPR $9^\circ 50' \text{ N}$ spreading rate of $10^{-1} \text{ m yr}^{-1}$), thus indicating that magma-hydrothermal activity in the EPR $9^\circ 50' \text{ N}$ area is episodic. Recent seismic data from the EPR between 8° and 11° N shows fluctuations in the depth to the AMC and variations in ridge axis morphology that are consistent with episodic magma replenishment (Carbotte et al., 2011). The estimated replenishment rate is similar to that determined for Axial Volcano on the Juan de Fuca Ridge between its eruption in 1998 (Nooner and Chadwick, 2009) and the eruption in April 2011 (Chadwick et al., 2011). Episodic magma-hydrothermal activity is consistent with diking episodes that occur during and between the major eruptions (Germanovich et al., 2011).

By comparing the chemical composition of lavas erupted in 1991–1992 with those erupted in 2005–2006, Goss et al. (2010) suggest that the AMC cooled approximately 20°C between these eruptions, and that the changes in lava composition cannot be explained by simple fractionation during crystallization. They suggest that replenishment by more evolved magma can account for the change in lava compositions over the eruption cycle. Horne et al. (2010) also derive liquid lines of descent for major elements using thermodynamic modeling software and confirm that simple fractionation cannot explain the evolution of

Table 2. Model-derived parameters for the EPR $9^\circ 50' \text{ N}$ magma-hydrothermal system

Symbol	Parameter	Value
Q_1	Mass flow in recharge	78 kg s^{-1}
Q_2	Mass flow in shallow recharge	$1,103 \text{ kg s}^{-1}$
Q_3	Mass flow in high-temperature vents	11 kg s^{-1}
Q_4	Mass flow from diffuse discharge	$1,170 \text{ kg s}^{-1}$
Q_1^*	Mass flow assuming H is all black smoker flow	86 kg s^{-1}
H_1	Heat output from axial magma chamber	$144 \pm 50\% \text{ MW}$
k_d	Permeability of discharge zone	$6 \times 10^{-13} \text{ m}^2$
δ	Thickness of conductive boundary layer	$14 \pm 50\% \text{ m}$
ξ	Mixing fraction of high-temperature fluid in diffuse flow	0.057
\dot{V}_m	Magma replenishment rate	$2 \times 10^6 \pm 50\% \text{ m}^3 \text{ yr}^{-1}$
τ	Fluid residence in discharge zone (using Darcian velocity)	1.5×10^7 to $1.5 \times 10^8 \text{ s}$

the erupted lavas. They suggest, however, that the evolution of erupted lavas over this time period involves a mixture of: (1) an aggregate primary mantle melt composition with some water emplaced at approximately 1,000 bars, cooling and fractionating over approximately a 60°C temperature interval, then migrating upward into the shallower AMC, and (2) an anhydrous or slightly hydrated residual liquid present in the AMC, with the additional possibility of the injection and eruption of the hydrous primary composition directly from 1,000 bars. The calculations of Horne et al. (2010) also suggest that between 50 and 90% of additional melt entered the AMC between the major eruptive events. Coupling these estimates with the modeling approach of Liu and Lowell (2009) suggests that the AMC grew from an initial thickness between 30 and 50 m in 1991 to approximately double its size by 2005. The model predicts a temperature decrease in the AMC of ~ 10°C. Although more work is needed to understand the chemical, thermal, and mechanical evolution of the AMC over an eruption cycle, the petrological data are generally consistent with models of magma convection and replenishment investigated by Liu and Lowell (2009).

Hydrothermal Recharge

The spatial and temporal location, extent, and evolution of hydrothermal recharge at ocean ridges have been elusive. In general, it is unclear whether recharge primarily occurs along or across axis, or whether it is fundamentally three dimensional. It is likely that recharge sites evolve with time as some regions get clogged with mineral precipitates such as anhydrite, and other regions open as a result of seismic and tectonic activity. As a result of its retrograde solubility, anhydrite may also dissolve in regions where the crust cools after sealing. Lowell and Yao (2002) argue that anhydrite precipitation would rapidly clog hydrothermal recharge zones unless the effective, time-integrated area of recharge was much larger than that of discharge. At EPR 9°50'N, Tolstoy et al. (2008) argue that recharge occurs through a relatively small area A_r at the seafloor of ~ 10⁵ m² south of TWP as delineated by seismicity (Figures 1 and 2). To test this idea, we use the one-dimensional model of Lowell and Yao (2002), employing the mass flow constraints for the EPR 9°50'N circulation cell obtained in the The Discharge Zone section above.

In the one-dimensional model, the thermal structure of the recharge zone

is found from the solution to the steady-state advection-diffusion heat transfer equation with uniform flow velocity and fixed temperatures at the top and bottom of the column (Bredehoeft and Papadopoulos, 1965). Assuming the temperature is $T = 0$ at the seafloor and $T = T_b$ at the base of the circulation cell, the temperature distribution is then

$$T_1(z) = T_b \frac{e^{(uz/a^*)} - 1}{e^{(uh/a^*)} - 1}, \quad (6)$$

where $u = Q_1/\rho_f A_r$ is the Darcian velocity; $h = 1.5$ km, corresponding to the depth to the AMC, is the height of the circulation cell; and $a^* = \lambda/\rho_f c_{it}$ is the effective thermal diffusivity (Table 1). Figure 6 plots temperature versus depth for two values of A_r (or u), assuming $T_b = 300^\circ\text{C}$. Anhydrite precipitates within the temperature region $150^\circ \leq T_1 \leq 300^\circ\text{C}$. The results show that if $A_r = 10^5$ m², which corresponds to the surface expression of recharge indicated by the shallow seismic data (Figure 1), the region of anhydrite precipitation is confined to the lowest 0.5 m of the recharge zone. If A_r is assumed to increase to 10⁶ m² at depth, the zone of potential anhydrite precipitation thickens to ~ 5 m. An effective increase in A_r at depth is consistent with the postulated flow lines shown in Figure 2.

Assuming thermodynamic equilibrium during anhydrite precipitation, the rate of change of porosity ϕ is given by

$$\frac{d\phi}{dt} = \frac{\rho_f u}{\rho_s} \frac{dC_{eq}}{dT} \frac{dT}{dz} \Big|_{z=h} \approx \frac{\rho_f u^2 T_b}{\rho_s a^*} \frac{dC_{eq}}{dT}, \quad (7)$$

where ρ_s is the density of anhydrite and dC_{eq}/dT is the rate of change in the solubility of anhydrite as a function of temperature. The temperature gradient was calculated from Equation 6.

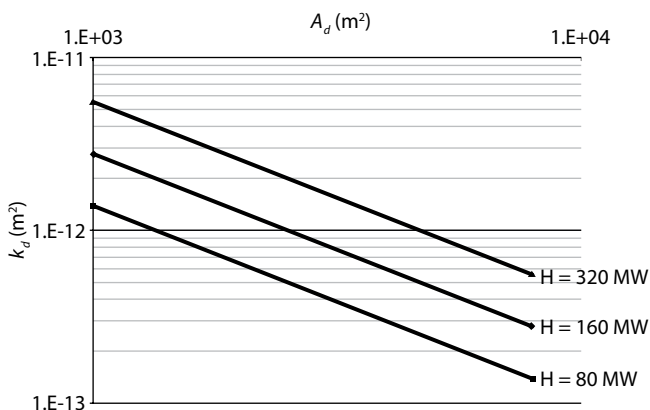


Figure 5. Plot of permeability k_d versus discharge area A_d for different values of total heat output H . The region between the solid lines shows the estimated value of permeability in the discharge zone taking into account the order of magnitude uncertainty in A_d and the factor of two uncertainty in the total heat output.

Integrating Equation 7 and assuming an initial porosity ϕ_0 in the region of anhydrite precipitation results in an approximate sealing time t_s . The results in Figure 7 show that if the recharge zone is treated as a simple, one-dimensional homogeneous region with $A_r \sim 10^5 \text{ m}^2$, it would seal rapidly, but if $A_r \sim 10^6 \text{ m}^2$, it would take significantly longer to seal, assuming the flow rate remains constant as the porosity is reduced. Initial porosity is likely to be in the range between 0.01 and 0.1. The TWP vent cooled and became inactive between 1994 and 2003, a decline that has been attributed to its proximity to the proposed recharge zone (Tolstoy et al., 2008). Other vents have remained rather steady, however, indicating that anhydrite precipitation has not generally clogged the system. This observation is consistent with an effective widening of the recharge zone with increasing depth.

To treat the hydrothermal recharge as a one-dimensional steady-state problem is a significant oversimplification. Micro-

earthquakes (Figure 2) may open new cracks, increasing permeability, but this effect is difficult to quantify. If the recharge zone is as small as postulated by Tolstoy et al. (2008), sealing would occur in a $\sim 0.5 \text{ m}$ thick region according to the one-dimensional model (Figure 6). It is not obvious that microseismicity in this narrow zone of precipitation would be sufficient to maintain permeability. It is also possible that recharge is focused along highly permeable flow paths that would seal rapidly as a result of anhydrite precipitation, thus forcing recharge flow to pass through regions of lower initial permeability. The overall evolution of crustal permeability in such a case has not yet been simulated.

NEXT STEPS

The temporal evolution of vent temperature and salinity in the hydrothermal system at EPR $9^\circ 50' \text{N}$ provides important insight into its dynamics, which are not addressed with the single-pass modeling approach presented here. For

example, perturbations of vent fluid temperature associated with seismic swarms may reflect perturbations in subsurface hydrology associated with minor diking events (Germanovich et al., 2011). Vent salinity data (Figure 3) indicate that phase separation is occurring within the crust, that vent salinities evolve with time, and that closely spaced vents such as Bio 9 and P may discharge vapor and brine salinities simultaneously. To address these issues, numerical modeling of two-phase flow is necessary. These models are in an early stage of development using NaCl-H₂O hydrothermal codes (e.g., Han, 2011), but at present it is not known whether the observed changes in vent salinity reflect changes in the subsurface heat source and/or crustal permeability, or whether they reflect natural fluctuations in a dynamic system.

In addition, models of magmatic heat flux from a crystallizing, replenished AMC described previously do not take into account details of magma

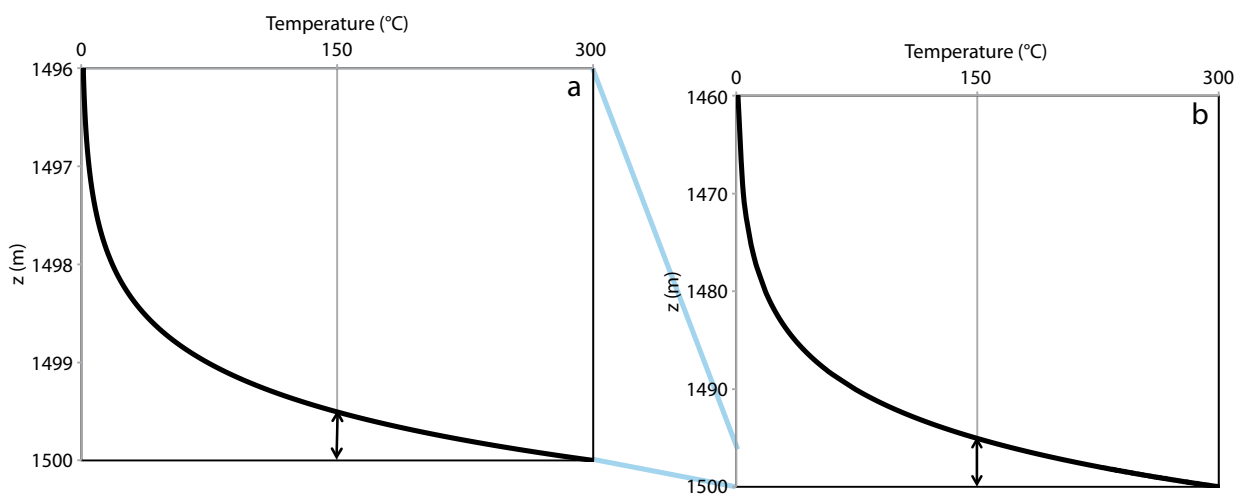


Figure 6. Plot of temperature versus depth in a one-dimensional recharge zone based on EPR 9°N parameters. Plot (a) assumes the recharge area $A_r = 10^5 \text{ m}^2$, corresponding to the surface area of recharge postulated by Tolstoy et al. (2008) (Figure 1). The zone of anhydrite precipitation denoted by the region starting with the double arrow to the base of the system is 0.5 m thick. Plot (b) assumes $A_r = 10^6 \text{ m}^2$, which is in keeping with the postulated flow paths shown in Figure 2. In this case, anhydrite precipitates over a wider zone, as shown. The blue lines highlight the change of scale between panels a and b.

fractionation, physical mechanisms of magma replenishment, and the possibility of partial melting and assimilation of overlying altered crust. The connections among AMC replenishment, infla-

precipitation during hydrothermal recharge is considerably more extensive than suggested by the one-dimensional model (Farough, 2011). Simulations that incorporate the evolution of

“GEOCHEMICAL DATA FROM BLACK SMOKERS AND NEARBY DIFFUSE-FLOW PATCHES, AS WELL AS AN ESTIMATE OF HEAT FLOW PARTITIONING, SUGGEST THAT NEARLY 90% OF THE HEAT OUTPUT STEMS FROM HEAT SUPPLIED BY THE SUBAXIAL MAGMA CHAMBER...”

tion, stress generation, and seismicity are yet to be quantified.

Finally, much more work is needed on reactive transport modeling and links between seismicity and hydrology. Initial results of numerical modeling of two-dimensional circulation in a homogeneous permeable medium suggest that the potential zone of anhydrite

permeability in the presence of micro-seismicity and anhydrite precipitation are needed to better understand the dynamics of recharge at EPR 9°50'N. Reactive transport models that link hydrothermal heat, mass, and chemical fluxes with biogeochemical processes also await development.

CONCLUSIONS

With the various data sets available from EPR 9°50'N, single-pass modeling approaches can provide considerable insight into physics of the magma-hydrothermal system. These approaches suggest that the bulk permeability of the discharge zone is $\sim 6 \times 10^{-13} \text{ m}^2$, with an uncertainty of approximately one order of magnitude. The thickness of the conductive boundary layer is $\sim 14 \text{ m} \pm 50\%$, and magma replenishment $\dot{V}_m \sim 2 \times 10^6 \pm 50\% \text{ m}^3 \text{ yr}^{-1}$ will stabilize heat hydrothermal vent temperatures and heat output on decadal time scales. This value of \dot{V}_m is in general accord with the evolution of lava chemistry over the eruption cycle between 1991–1992 and 2005–2006. One-dimensional models of hydrothermal recharge suggest that a recharge area of 10^5 m^2 as indicated by shallow seismicity would rapidly seal with anhydrite, but if the recharge zone broadens at depth to $\sim 10^6 \text{ m}^2$, anhydrite precipitation may not affect circulation. More-realistic models of hydrothermal recharge that incorporate the effects of anhydrite precipitation in a two- or three-dimensional circulation system that has heterogeneous permeability, and models that link seismicity with permeability, are needed.

Although a broad spectrum of data is used to constrain these results, lack of data, particularly on heat output and area of diffuse flow sites, and possibly on the temporal variability of heat output, results in considerable uncertainty in key parameters. Much remains to be done, both in terms of modeling and in data acquisition. Hopefully, the models presented here will guide future developments at this key hydrothermal site.

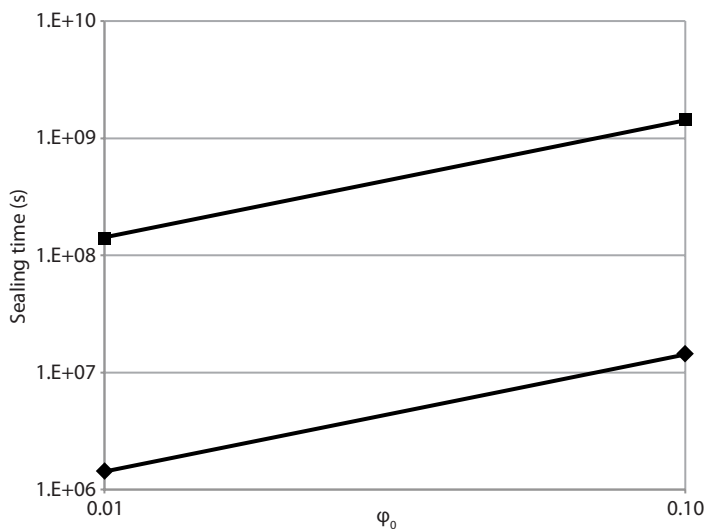


Figure 7. Plot of sealing time in seconds versus initial porosity for two different values of recharge area A_r .

ACKNOWLEDGMENTS

We thank Andy Fisher and an anonymous reviewer for their thorough and insightful reviews. Liang Han provided useful insights regarding modeling of phase separation. Lei Liu provided calculations on magma convection and replenishment that shaped the ideas presented here. This research has been supported in part by NSF grant 0926418 to RPL. 

REFERENCES

- Baker, E.T. 2007. Hydrothermal cooling of midocean ridge axes: Do measured and modeled heat fluxes agree? *Earth and Planetary Science Letters* 263:140–150, <http://dx.doi.org/10.1016/j.epsl.2007.09.010>.
- Bemis, K., R.P. Lowell, and A. Farough. 2012. Diffuse flow on and around hydrothermal vents at mid-ocean ridges. *Oceanography* 25(1):182–191, <http://dx.doi.org/10.5670/oceanog.2012.16>.
- Bredehoeft, J.D., and I.S. Papadopoulos. 1965. Rates of vertical groundwater movement estimated from the Earth's thermal profile. *Water Resources Research* 1:325–328, <http://dx.doi.org/10.1029/WR001i002p00325>.
- Carbotte, S.M., M. Marjanovic, H.D. Carton, J.C. Mutter, J.P. Canales, M. Xu, M.R. Nedimović, and O. Aghaei. 2011. The ups and downs of magma in the crust beneath the East Pacific Rise axis 8°20'–10°10'N. *Eos, Transactions, American Geophysical Union* 92(52):Fall Meeting Abstract OS22A-01.
- Chadwick, B., S.L. Nooner, D.A. Butterfield, M.D. Lilley, D.A. Clague, D.W. Caress, R.P. Dziak, and J.H. Haxel. 2011. Discovery of the 2011 eruption at Axial Seamount. *Eos, Transactions, American Geophysical Union* 92(52):Fall Meeting Abstract V14C-04.
- Craft, K., and R.P. Lowell. 2009. A boundary layer model for submarine hydrothermal flows at on-axis and near axis locations. *Geochemistry Geophysics Geosystems* 10, Q12012, <http://dx.doi.org/10.1029/2009GC002707>.
- Crowell, B.W., R.P. Lowell, and K.L. Von Damm. 2008. A model for the production of sulfur flow and “snowblower” events at mid-ocean ridges. *Geochemistry Geophysics Geosystems* 9, Q10T02, <http://dx.doi.org/10.1029/2008GC002103>.
- Crone, T.J., M. Tolstoy, and D.F. Stroup. 2011. Permeability structure of young oceanic crust from poroelastically triggered earthquakes. *Geophysical Research Letters* 38, L05305, <http://dx.doi.org/10.1029/2011GL046820>.
- Detrick, R.S., P. Buhl, E. Vera, J. Mutter, J. Orcutt, J. Madsen, and T. Brocher. 1987. Multi-channel seismic imaging of a crustal magma chamber along the East Pacific Rise. *Nature* 326: 35–41, <http://dx.doi.org/10.1038/326035a0>.
- Farough, A. 2011. A parameterized approach to partitioning between focused and diffuse heat output and modeling hydrothermal recharge at the East Pacific Rise 9°50'N. MS Thesis, Virginia Tech, Blacksburg, VA.
- Ferrini, V.L., D.J. Fornari, T.M. Shank, J.C. Kinsey, M.A. Tivey, J.A. Soule, S.M. Carbotte, L.L. Whitcomb, D. Yoerger, and J. Howland. 2007. Sub-meter bathymetric mapping of volcanic and hydrothermal features on the East Pacific Rise crest 9°50'N. *Geochemistry Geophysics Geosystems* 8, Q01006, <http://dx.doi.org/10.1029/2006GC001333>.
- Fornari, D.J., K.L. Von Damm, J.G. Bryce, J.P. Cowen, V. Ferrini, A. Fundis, M.D. Lilley, G.W. Luther III, L.S. Mullineaux, M.R. Perfit, and others. 2012. The East Pacific Rise between 9°N and 10°N: Twenty-five years of integrated, multidisciplinary oceanic spreading center studies. *Oceanography* 25(1):18–43, <http://dx.doi.org/10.5670/oceanog.2012.02>.
- Germanovich, L.N., R.P. Lowell, and P. Ramondenc. 2011. Magmatic origin of hydrothermal response to earthquake swarms: Constraints from heat flow and geochemical data at 9°50'N, East Pacific Rise. *Journal of Geophysical Research* 116, B05103, <http://dx.doi.org/10.1029/2009JB006588>.
- Goss, A.R., M.R. Perfit, W.I. Ridley, K.H. Rubin, G.D. Kamenov, S.A. Soule, A. Fundis, and D.A. Fornari. 2010. Geochemistry of lavas from the 2005–2006 eruption at the East Pacific Rise (9°46'–56'N): Implications for ridge crest plumbing and decadal changes in magma chamber compositions. *Geochemistry Geophysics Geosystems* 11, Q05T09, <http://dx.doi.org/10.1029/2009GC002977>.
- Han, L. 2011. Exploring two-phase hydrothermal circulation at a seafloor pressure of 25 MPa: Application for EPR 9°50'N. MS Thesis, Virginia Tech, Blacksburg, VA.
- Horne, R., L. Hebert, L. Liu, and R. Lowell. 2010. Fractional crystallization and replenishment of the magma chamber at the East Pacific Rise 9°50'N. *Eos, Transactions, American Geophysical Union* 91(52):Fall Meeting Abstract OS21C-1507.
- Kent, G.M., A.J. Harding, and J.A. Orcutt. 1990. Evidence for a smaller magma chamber beneath the East Pacific Rise at 9°30'N. *Nature* 344:650–653, <http://dx.doi.org/10.1038/344650a0>.
- Liu, L., and R.P. Lowell. 2009. Models of hydrothermal heat output from a convecting, crystallizing, replenished magma chamber beneath an oceanic spreading center. *Journal of Geophysical Research* 114, B02102, <http://dx.doi.org/10.1029/2008JB005846>.
- Lowell, R.P., and L.N. Germanovich. 2004. Seafloor hydrothermal processes: Results from scale analysis and single-pass models. Pp. 219–244 in *Mid-Ocean Ridges: Hydrothermal Interactions Between the Lithosphere and Oceans*. C.R. German, J. Lin, and L.M. Parson, eds, Geophysical Monograph Series, vol. 148, American Geophysical Union, Washington, DC.
- Lowell, R.P., and Y. Yao. 2002. Anhydrite precipitation and the extent of hydrothermal recharge zones at ocean ridge crests. *Journal of Geophysical Research* 107, 2183, <http://dx.doi.org/10.1029/2001JB001289>.
- Nooner, S.L., and W.W. Chadwick Jr. 2009. Volcanic inflation measured in the caldera of Axial Seamount: Implications for magma supply and future eruptions. *Geochemistry Geophysics Geosystems* 10, Q02002, <http://dx.doi.org/10.1029/2008GC002315>.
- Ramondenc, P., L.N. Germanovich, K.L. Von Damm, and R.P. Lowell. 2006. The first measurements of hydrothermal heat output at 9°50'N, East Pacific Rise. *Earth and Planetary Science Letters* 245:487–497, <http://dx.doi.org/10.1016/j.epsl.2006.03.023>.
- Sohn, R.A., D.J. Fornari, K.L. Von Damm, J.A. Hildebrand, and S.C. Webb. 1998. Seismic and hydrothermal evidence for a cracking event on the East Pacific Rise crest at 9°50'N. *Nature* 396:159–161, <http://dx.doi.org/10.1038/24146>.
- Tolstoy, M., F. Waldhauser, D.R. Bohnenstiehl, R.T. Weekly, and W.Y. Kim. 2008. Seismic identification of along-axis hydrothermal flow on the East Pacific Rise. *Nature* 451:181–187, <http://dx.doi.org/10.1038/nature06424>.
- Von Damm, K.L. 2004. Evolution of the hydrothermal system at East Pacific Rise 9°50'N: Geochemical evidence for changes in the upper oceanic crust. Pp. 285–305 in *Hydrothermal Interactions between the Lithosphere and Oceans*. C.R. German, J. Lin, and L.M. Parson, eds, Geophysical Monograph Series, vol. 148, American Geophysical Union, Washington, DC.
- Von Damm, K.L., and M.D. Lilley. 2004. Diffuse flow hydrothermal fluids from 9°50'N East Pacific Rise: Origin, evolution, and biogeochemical controls. Pp. 245–268 in *The Subseafloor Biosphere at Mid-Ocean Ridges*. W.S. Wilcock, E.F. DeLong, D.S. Kelley, J.A. Baross, and S.C. Cary, eds, Geophysical Monograph Series, vol. 144, American Geophysical Union, Washington, DC.